MESSENGER

Mercury's magnetosphere-solar wind interaction for northward and southward interplanetary magnetic field during the MESSENGER Flybys

P. M. Trávníček[1,3], D. Schriver[2], D. Herčík[3], P. Hellinger[3], J. Páral[3,4], B. J. Anderson[5], S. M. Krimigis[5], R.L. McNutt Jr.[5], Y. Saito[6], J. A. Slavin[7], S. C. Solomon[8]

[1] Space Science Laboratory, UCB, Berkeley, CA, USA; [2] Institute of Geophysics and Planetary Physics, UCLA, Los Angeles, CA, USA; [3] Astronomical Institute and Institute of Atmospheric Physics, ASCR, Prague, Czech Republic; [4] Department of Physics, UoA, Edmonton, Canada; [5] Heliophysics Science Division, NASA GSFC, Greenbelt, MD, USA; [6] ISAS/JAXA, Sagamihara, Kanagawa 229-8510, Japan; [7] The Johns Hopkins University Applied Physics Laboratory, Laurel, MD, USA; [8] Department of Terrestrial Magnetism, Carnegie Institution of Washington, D.C;

MESSENGER/BepiColombo meeting, Boulder, November, 2010

Solar wind expansion:

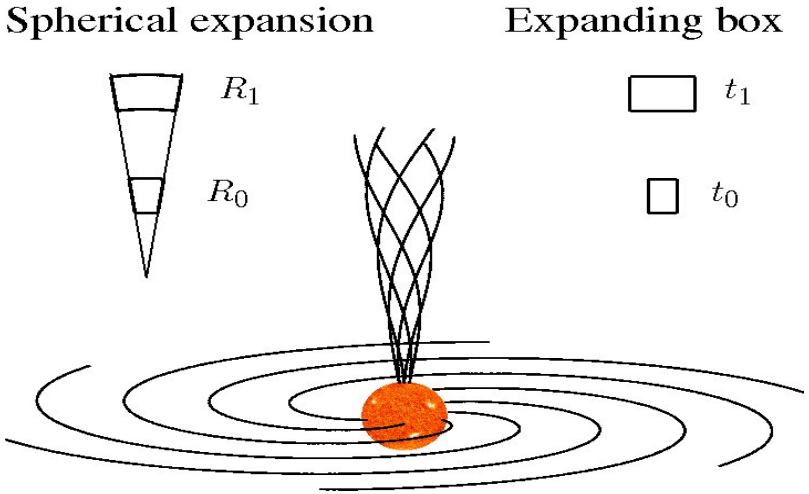

- A homogeneous slowly expanding plasma (without any fluctuating wave energy) evolves adiabatically. The ion parallel and perpendicular temperatures $T_{\parallel}$ and $T_{\perp}$ satisfy the CGL equations $T_{\parallel} \propto B$ and $T_{\perp} \propto n^2/B^2$, respectively.
- Plasma temperature anisotropies naturally develop. Temperature anisotropy (i.e. departure from Maxwellian particle distribution function) represent a possible source of free energy for many different instabilities.

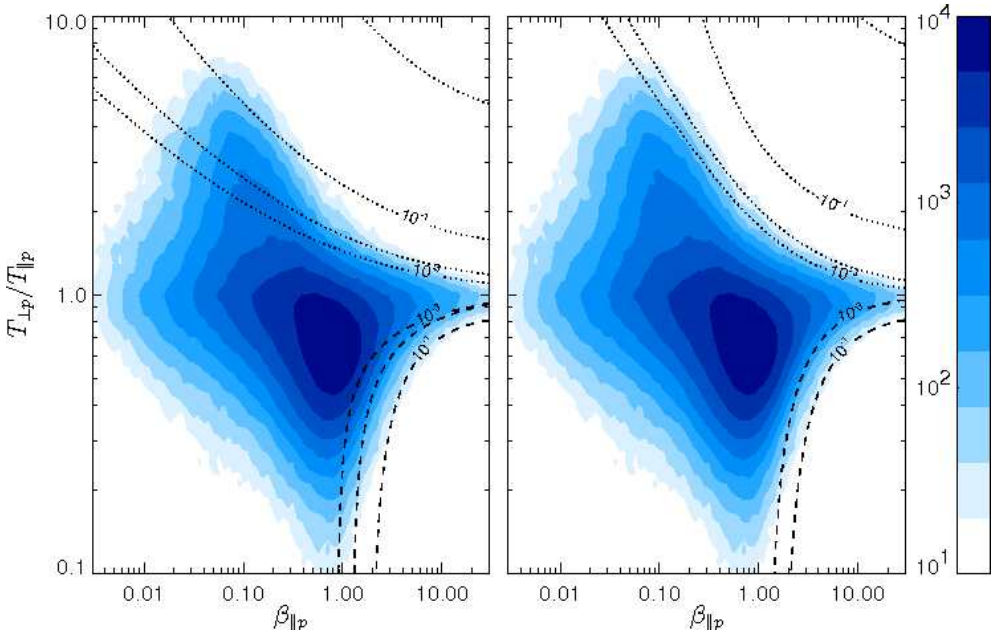

(*Hellinger et al.*, 2006)

- Both panels show a color scale plot of the relative frequency of $(\beta_{p\parallel}, T_{p\perp}/T_{p\parallel})$ in the WIND/SWE data (1995-2001) for the solar wind $v_{\mathrm{SW}} < 600$ km/s
- The over plotted curves show the contours of the maximum growth rate (in units ω_{cp}) in the corresponding bi-Maxwellian plasma
  - proton cyclotron instability (solid curves)
  - parallel fire hose instability (dashed curves)
  - proton mirror instability (dotted curves)
  - oblique fire hose instability (dash-dotted curves)

Magnetosheath plasma:

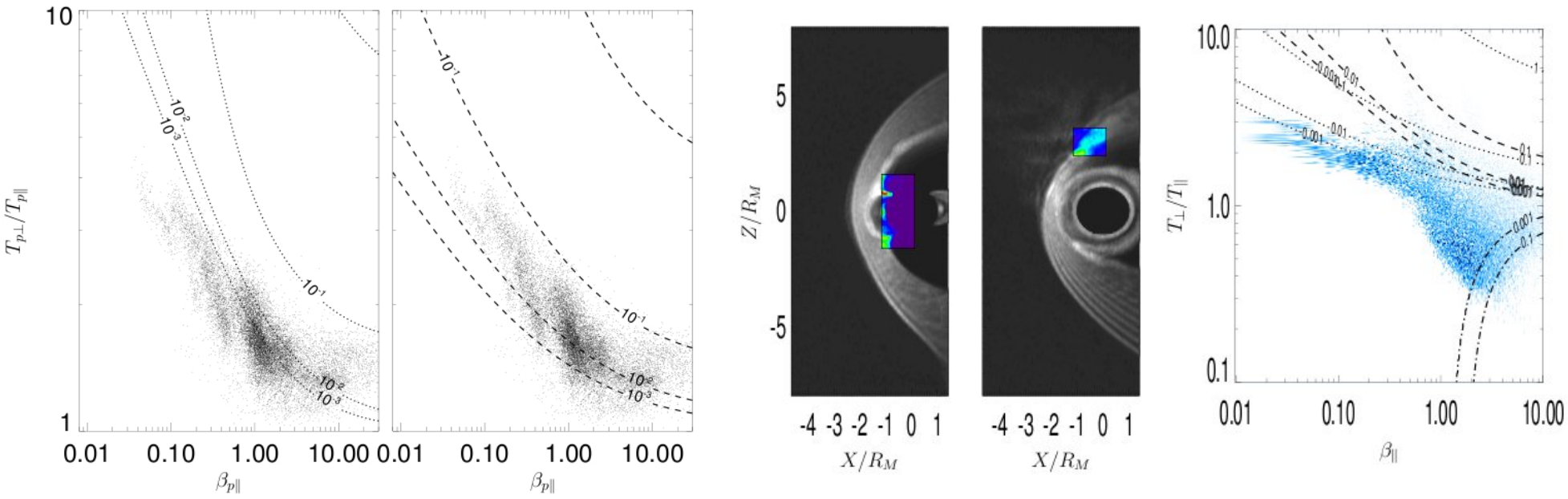

LEFT: *In situ* observations made by HIA experiment on Cluster II (*Travnicek et al.*, 2007), RIGHT: simulated magnetosheat plasma.

Some qualitative agreement ...:

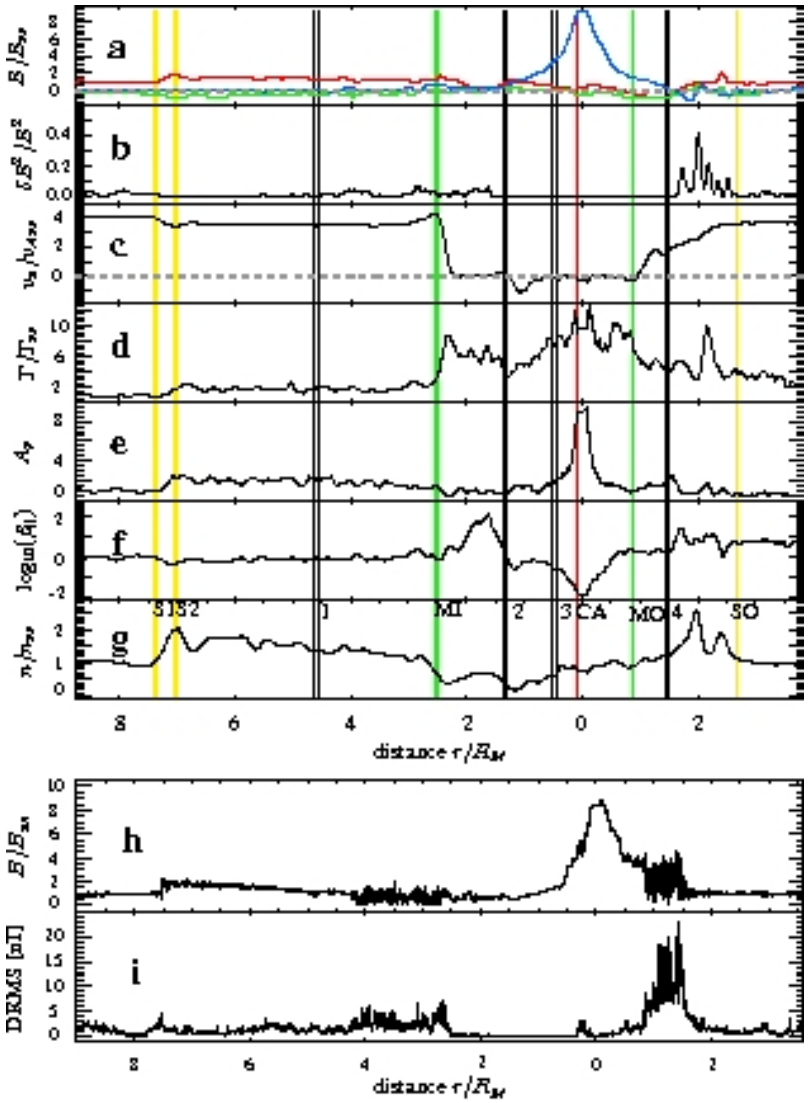

Figure 1: Upper panels shows several observables from a global simulation along virtual M1 flyby trajectory of virtual MESSENGER.

Bottom panel shows *in situ* observed magnitude of the magnetic field and the amplitude of magnetic field oscilations.

(*Travnicek et al.*, 2009)

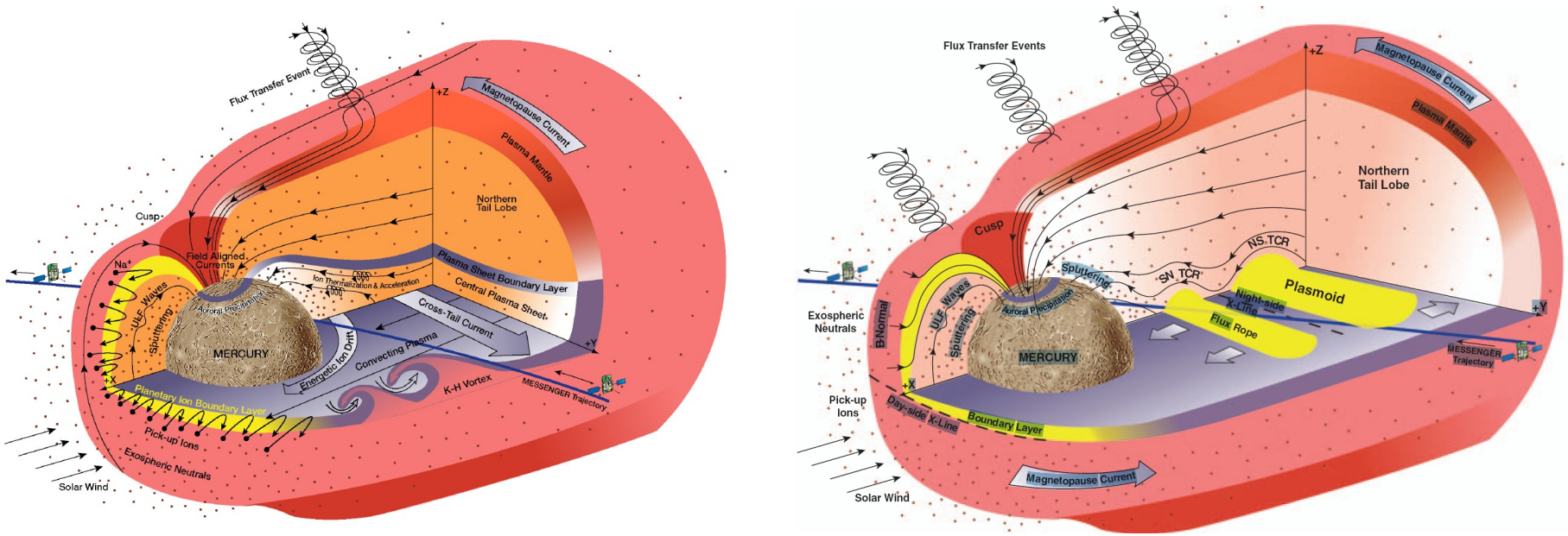

Figure 2: Schematic views of Mercury's magnetosphere for (left) a northward IMF highlighting the features and phenomena observed by MESSENGER during its flyby of 14 January 2008 (from *Slavin et al.*, 2008) and for (right) a southward IMF as observed by MESSENGER on 6 October 2008 (from *Slavin et al.*, 2009).

	run Hyb1	run Hyb2
Spatial resolution Δx	$0.4\ d_{psw}$	
Spatial resolution $\Delta y = \Delta z$	$1.0\ d_{psw}$	
Spatial size of the system $L_x = N_x \Delta x$	$237.6\ d_{psw}$	
Spatial size of the system $L_y = L_z = N_y \Delta y$	$288\ d_{psw}$	
Mercury's radius R_M	$15.32\, d_{psw}$	
Temporal resolution (simulation time step) Δt	$0.02\ \omega_{gpsw}^{-1}$	
Time sub-stepping for electromagnetic fields Δt_B	$\Delta t/20 = 0.001\ \omega_{gpsw}^{-1}$	
Simulation box transition time	$59.4\ \omega_{gpsw}^{-1}$	
Duration of each simulation	$120.0\ \omega_{gpsw}^{-1}$	
β_{psw}	1.0	
β_{esw}	1.0	
Number of macro-particles per cell (specie 0)	80	50
Number of macro-particles per cell (specie 1)	100	100
Total number of macro-particles	$\sim 3.9\times10^9$	$\sim 2.5\times10^9$
Solar wind velocity v_{psw}	$4.0\ v_{Asw}$	
Orientation of IMF in (X,Z) plane	+ 20°	- 20°
Mercury's magnetic moment M	250 nT $R_M^3\, 4\pi/\mu_0$ (no tilt)	
n_{psw}, B_{sw}, v_{Asw}, d_{psw}, ω_{gpsw}	= 1 (in simulation units)	

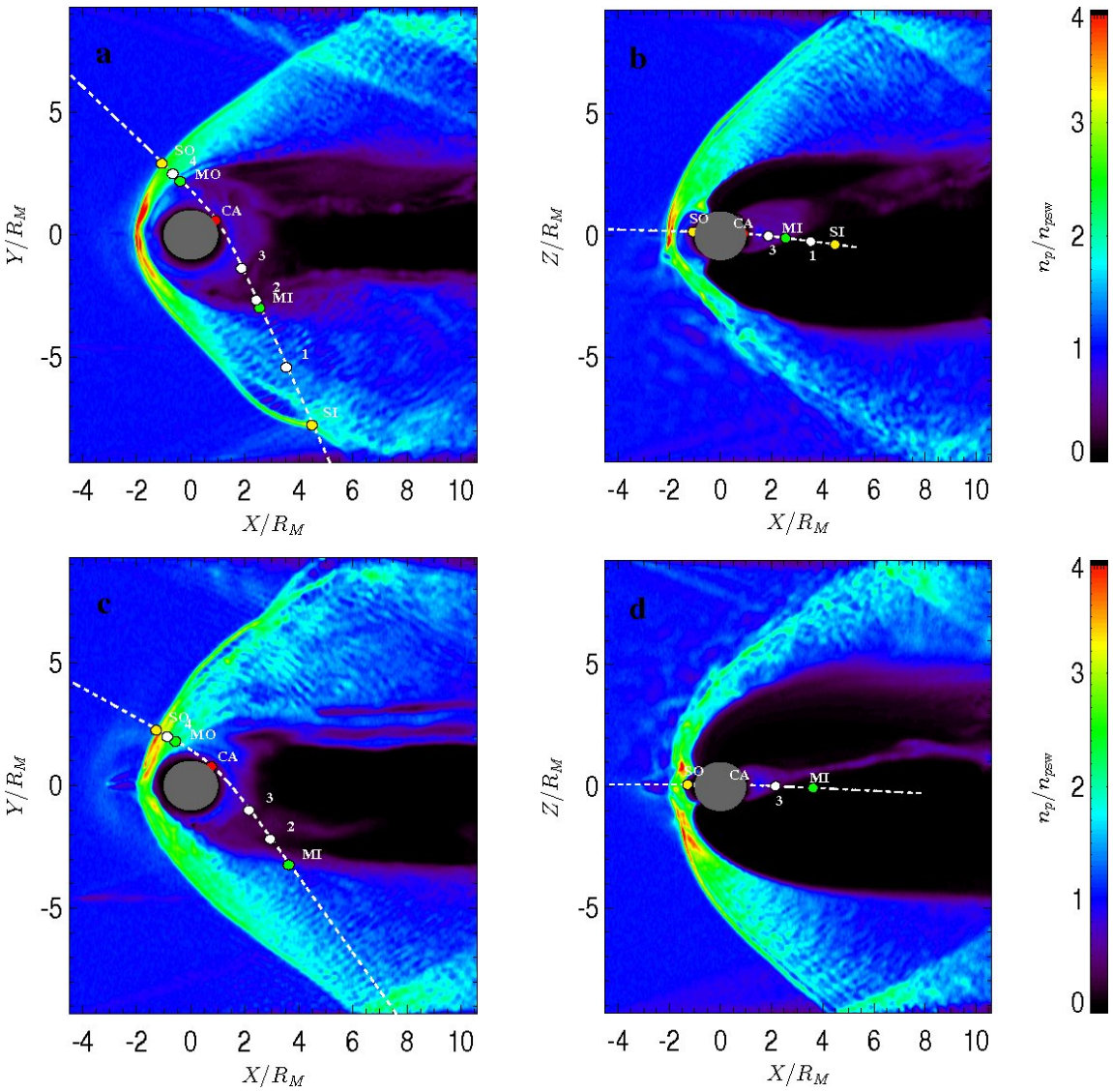

Figure 3: Upper panels show the simulated proton density n_p in two planes: (a) the equatorial plane (X,Y) and (b) the plane of main meridian (X,Z) from simulation Hyb1 (northward IMF) at $t = 100\,\omega_{gpsw}^{-1}$. Bottom panels (c) and (d) show the same information from simulation Hyb2 (southward IMF).

Table: List of markers used for the orientation along the (virtual) M1 and M2 trajectories

Marker	description	color	r/R_M for M1	r/R_M for M2
"SI"	shock inbound	yellow	8.0	-
"1"		white	5.5	-
"MI"	magnetopause inbound	green	2.9	3.9
"2"		white	2.6	2.7
"3"		white	1.3	1.4
"CA"	closest approach	red	0.1	0.1
"MO"	magnetopause inbound	green	1.2	0.9
"4"		white	1.6	1.2
"SO"	shock outbound	yellow	2.1	1.6

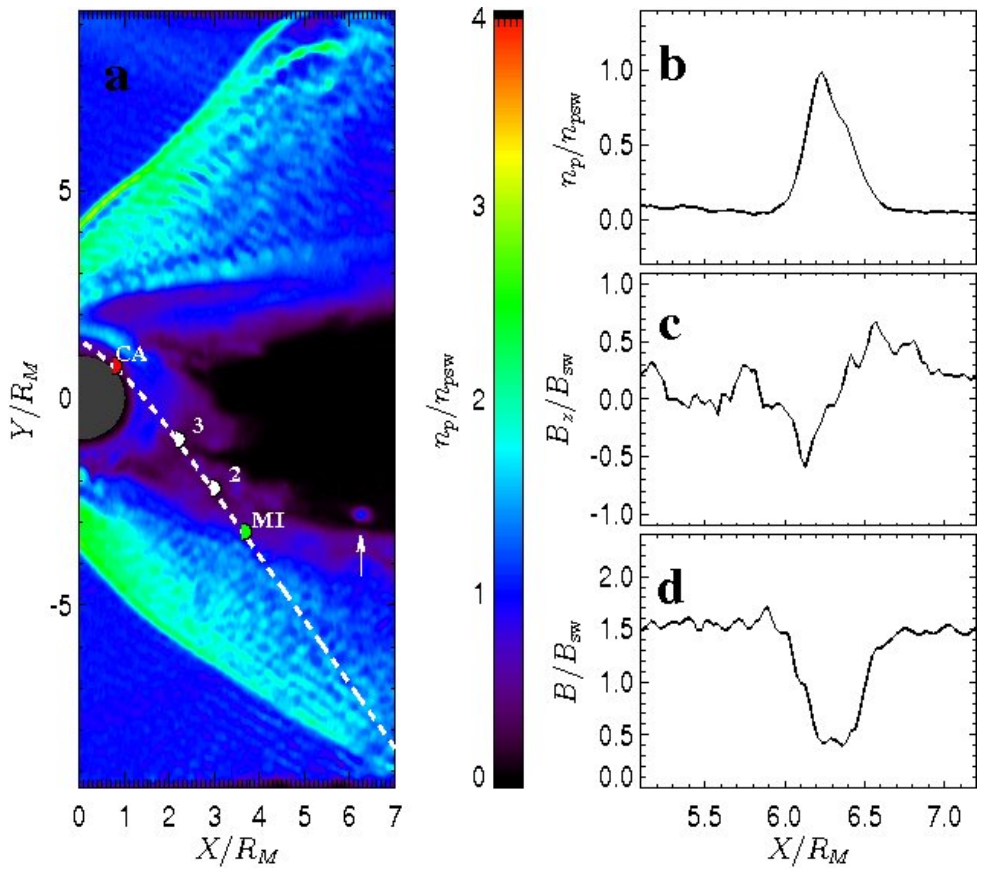

Figure 4: An example of a plasmoid formed in the magnetotail marked by a white arrow on panel (a) which shows simulated proton density n_p in the equatorial plane (X, Y) (southward IMF). The plasmoid structure has roughly $0.5\,R_M$ in diameter (see panels b-d) and its life-span from time of its formation to its dissipation is $\approx 10 - 20\,\omega_{gpsw}^{-1}$. The plasmoid tends to move slowly down the magnetotail away from the planet.

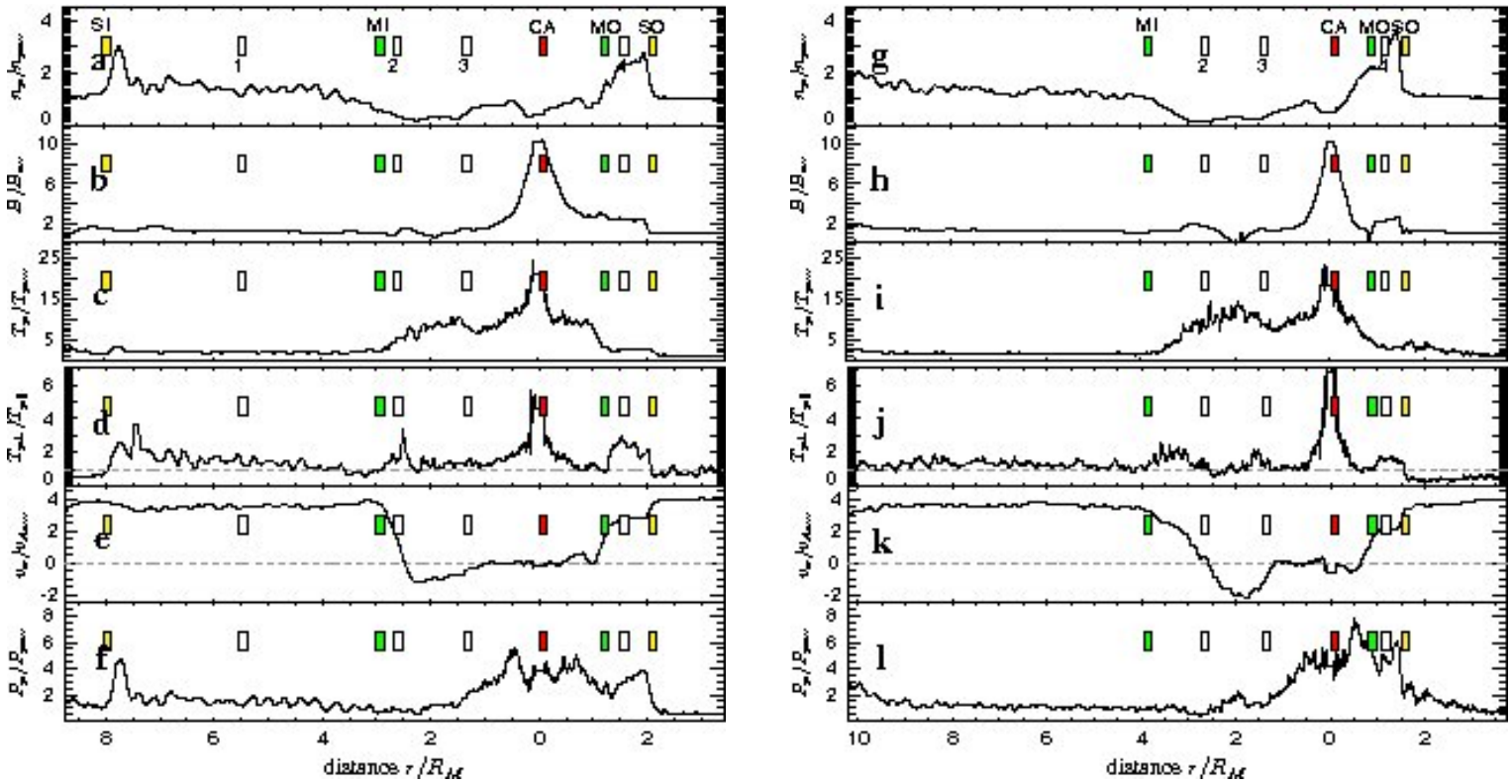

Figure 5: Panels a and g show the density n_p/n_{psw}, panels b and h show magnitude of the magnetic field B/B_{sw}, panels c and i display the proton plasma temperature T_p/T_{psw}, panels d and j show the proton temperature anisotropy $T_{p\perp}/T_{p\|}$, panels e and k show the X-component of the plasma bulk velocity v_{px}/v_{Apsw}, and panels f and l displays the proton kinetic pressure p_p/p_{psw}.

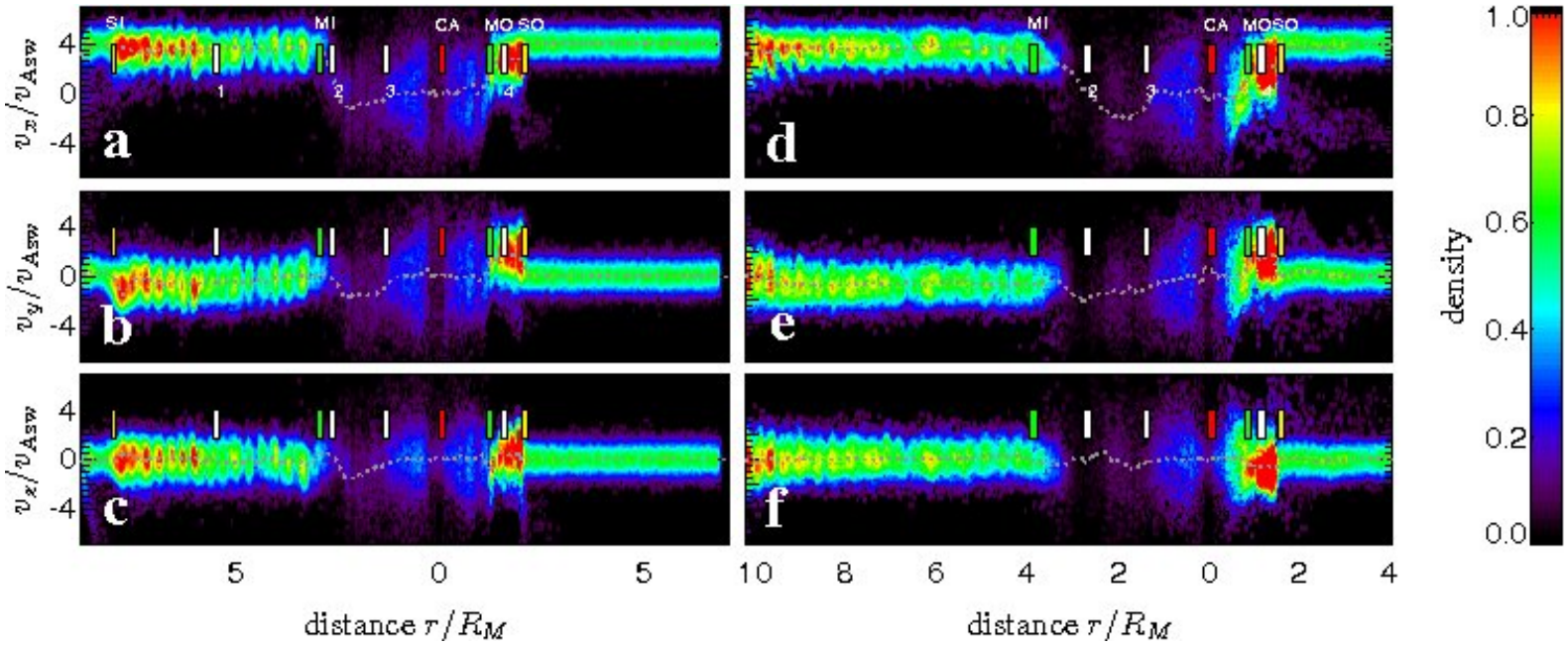

Figure 6: Proton velocity distribution function f_p along the M1 trajectory from simulation Hyb1 with northward IMF (left panels) and along the M2 trajectory in simulation Hyb2 with southward IMF (right panels). Panels show different cuts of f_p calculated along the corresponding spacecraft trajectory from all macro-particles within a sphere with radius $r_{\mathrm{vdf}} = 0.9 d_{\mathrm{psw}}$.

Figure 7: Density of ions ejected from Hermean surface $v_{psw} = 5v_{Asw}$ vs. $v_{psw} = 3v_{Asw}$ (in units of 10^{-4} n_{psw}) (*Travnicek et al.*, 2008):

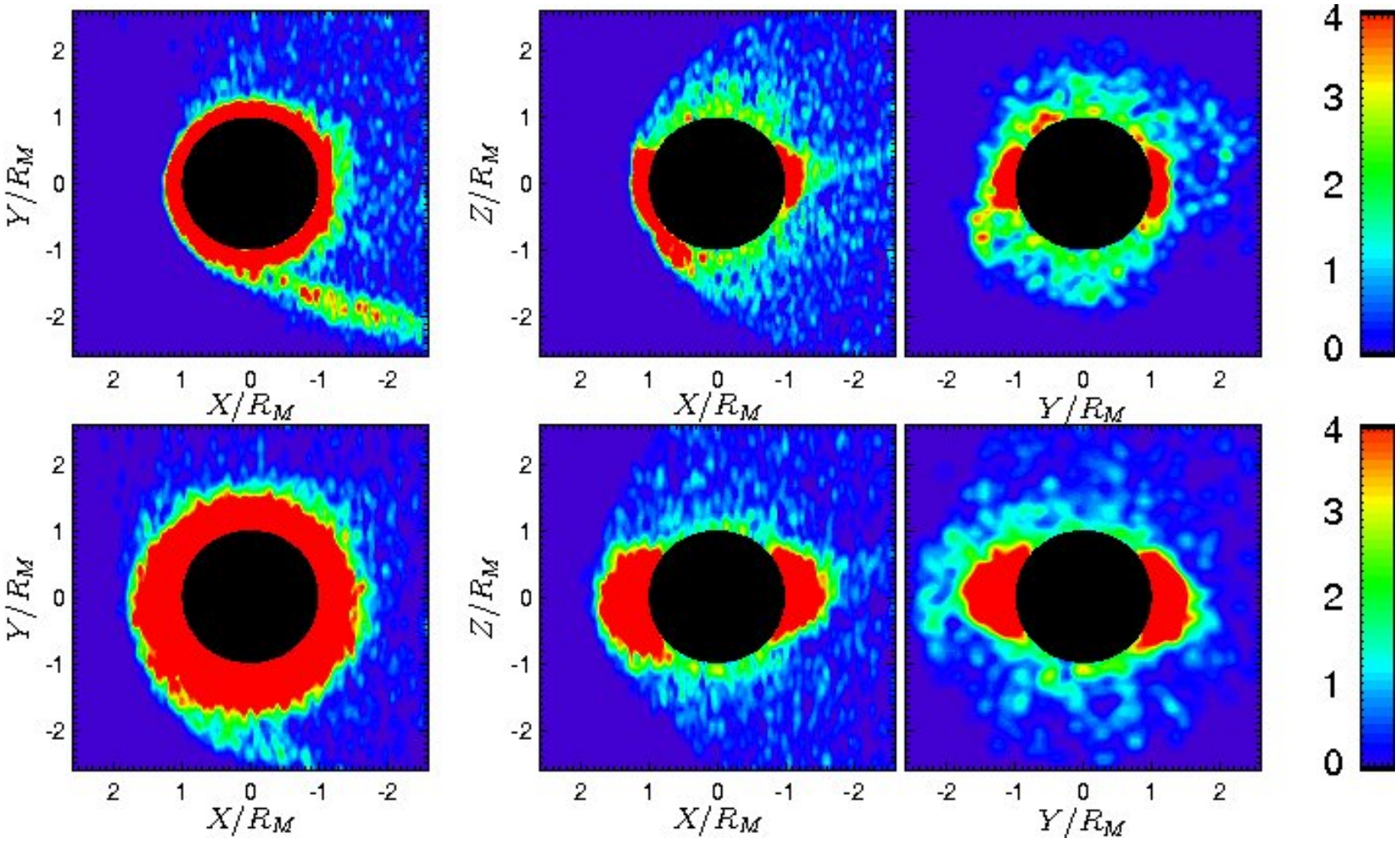

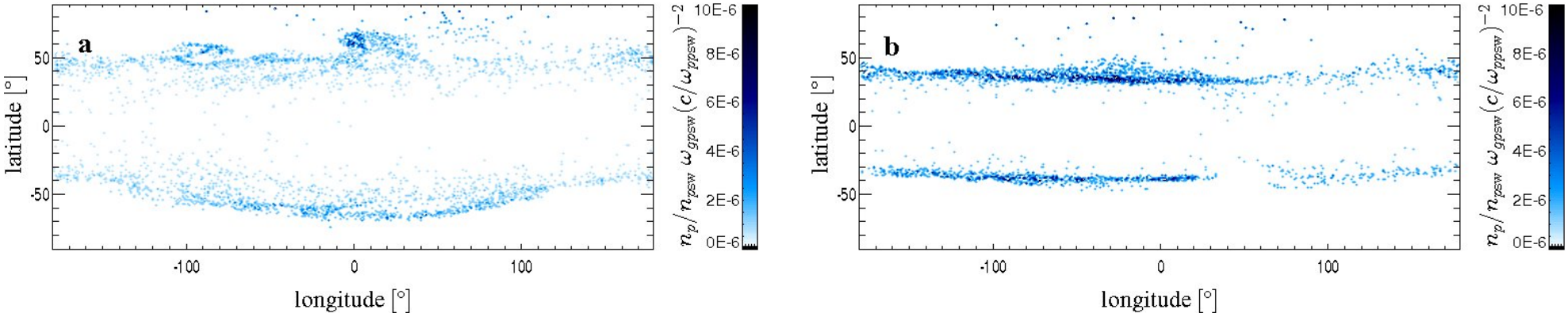

Figure 8: Precipitation of solar wind protons onto the surface of Mercury as seen in our simulation with (a) northward IMF and with (b) southward IMF. Macro-particles were collected over a time period of $\Delta T = \omega_{gp\mathrm{sw}}^{-1}$ at $t = 100\ \omega_{gp\mathrm{sw}}^{-1}$. The longitude 0° and the latitude 0° correspond to the dayside subsolar point. Both panels show the number of protons n_p in the units of the solar wind proton density $n_{p\mathrm{sw}}$ absorbed by Mercury's surface at the given location per accumulation time $\omega_{gp\mathrm{sw}}^{-1}$ per $(c/\omega_{pp\mathrm{sw}})^2$.

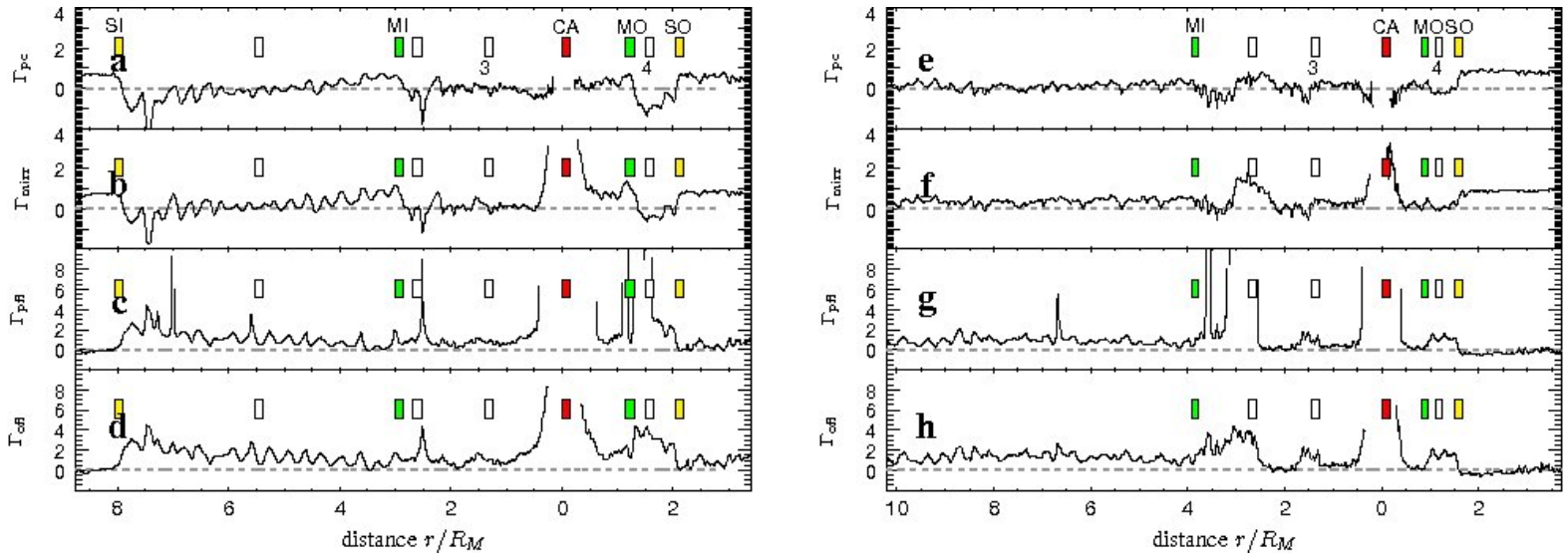

Figure 9: Distance from marginal stability criteria given by

$$\Gamma = \mathrm{sgn}(a)\left(\frac{a}{(\beta_{\|p}-\beta_0)^b} - \frac{T_{\perp p}}{T_{\|p}} + 1\right)$$

along spacecraft trajectory M1 in simulation Hyb1 (left panels) and along M2 in Hyb2 (right panels) for (a and e) the proton cyclotron instability, Γ_{pc}, (b and f) the mirror instability, Γ_{mir}, (c and g) the parallel fire hose, Γ_{pf}, and (d and h) the oblique fire hose, Γ_{of}.

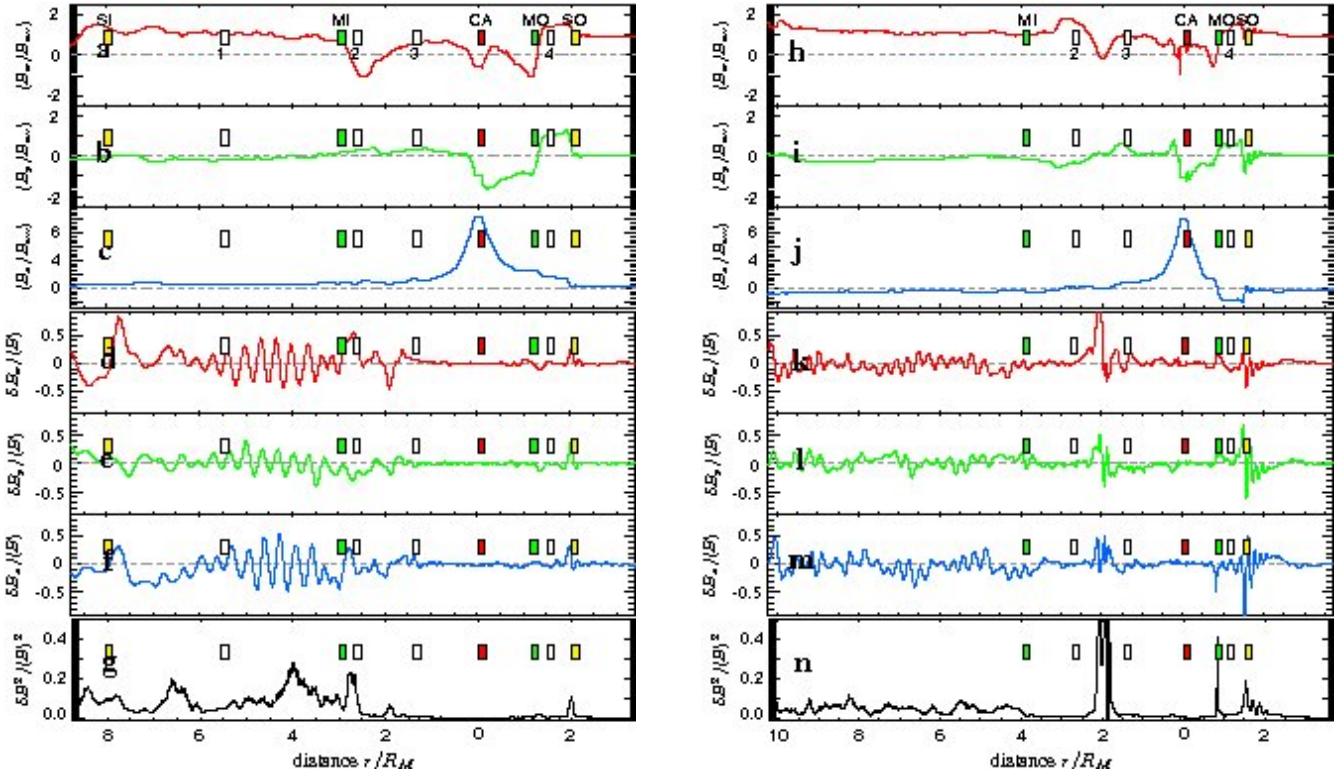

Figure 10: On first six panels the three time-averaged magnetic components are shown: $\langle B_x \rangle$ (a/h, red line), $\langle B_y \rangle$ (b/i, green line), and $\langle B_z \rangle$ (c/j, blue line). The second six panels displays relative variations of the three magnetic components from the averaged value at time $t = 100\,\omega_{gpsw}^{-1}$ $\delta B_x/\langle B \rangle$ (d/k, red line), $\delta B_y/\langle B \rangle$ (e/l, green line), and $\delta B_z/\langle B \rangle$ (f/m, blue line). The last two panels (g/n) show the relative fluctuating magnetic energy $\delta B^2/\langle B \rangle^2$.

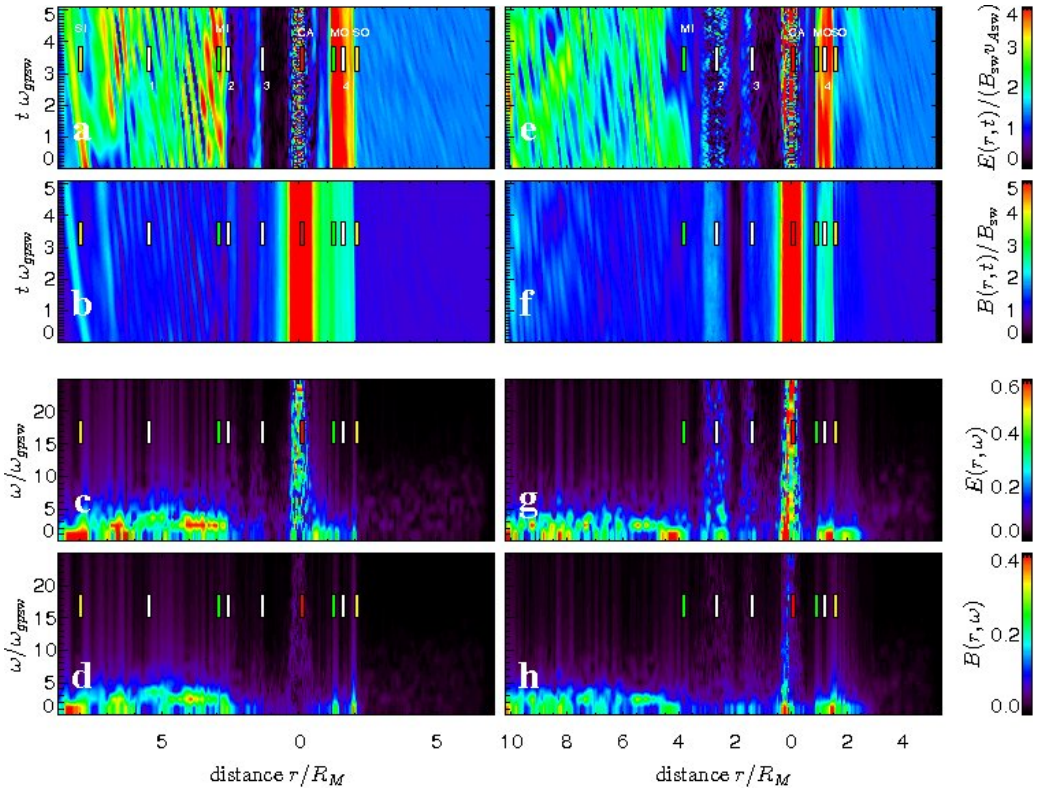

Figure 11: Time evolution of the absolute value of (a and e) electric $E(r,t)/(B_{\rm sw}v_{A\rm sw})$ and (b and f) magnetic $B(r,t)/B_{\rm sw}$ fields and the corresponding spectra (c and g) $E(r,\omega)$ and (d and h) $B(r,\omega)$ from simulation Hyb1 with northward IMF along the M1 trajectory (left) and from simulation Hyb2 with southward IMF along the M2 trajectory (right).

Figure 12: Cross correlation $\langle B, n \rangle$ (south-ward IMF):

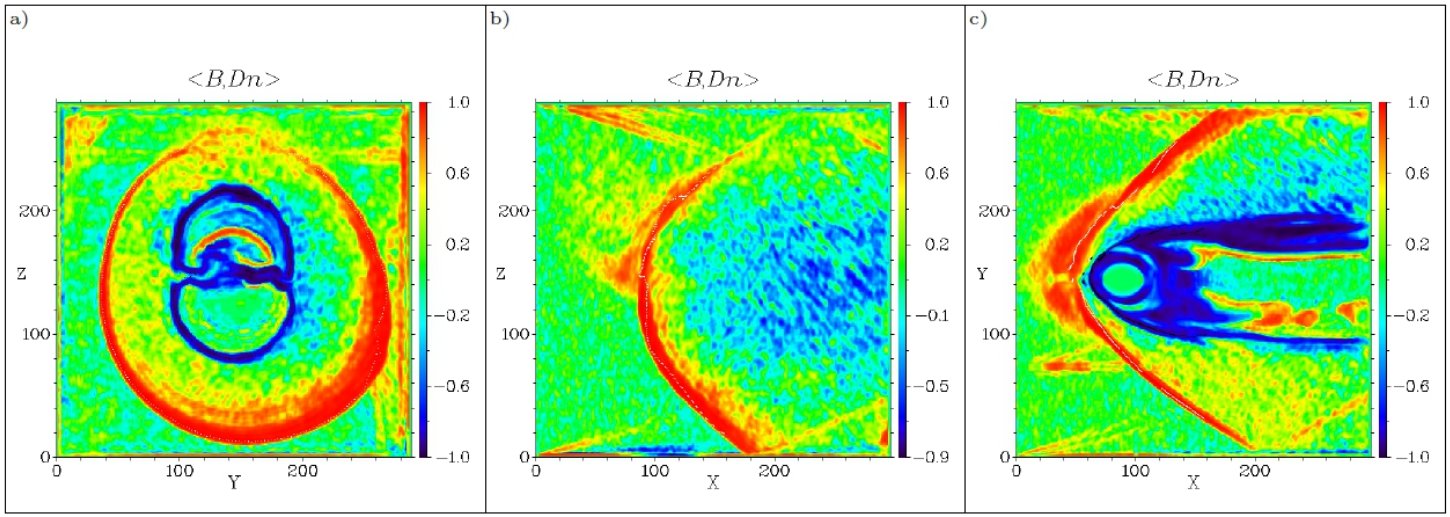

Figure 13: Compressibility $\delta B_{\parallel}^2 / \delta B_{\perp}^2$ (south-ward IMF):

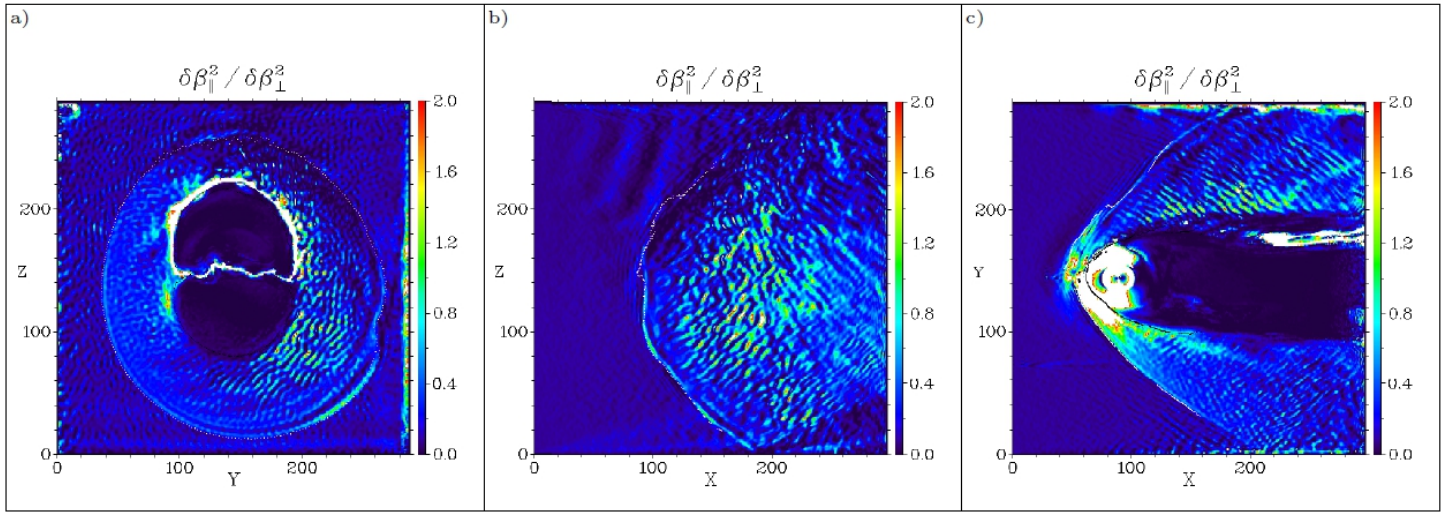

MESSENGER

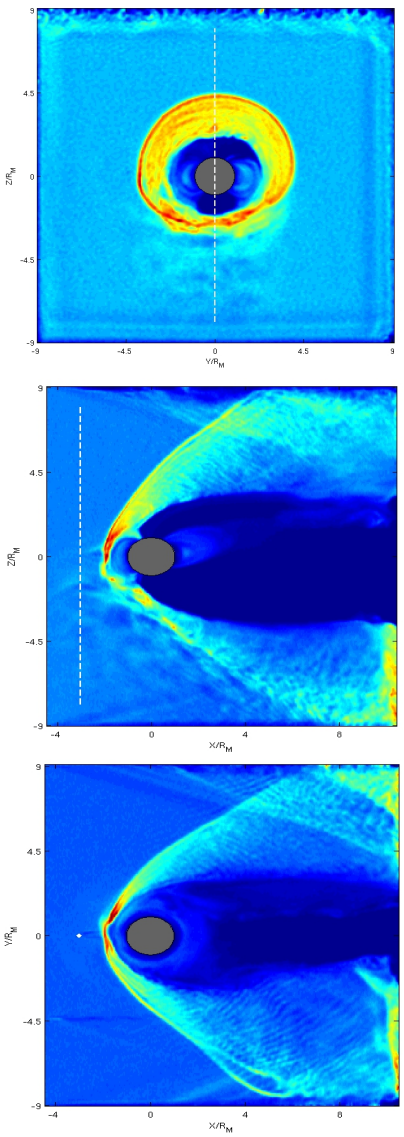
Z/R_M
Y/R_M
X/R_M

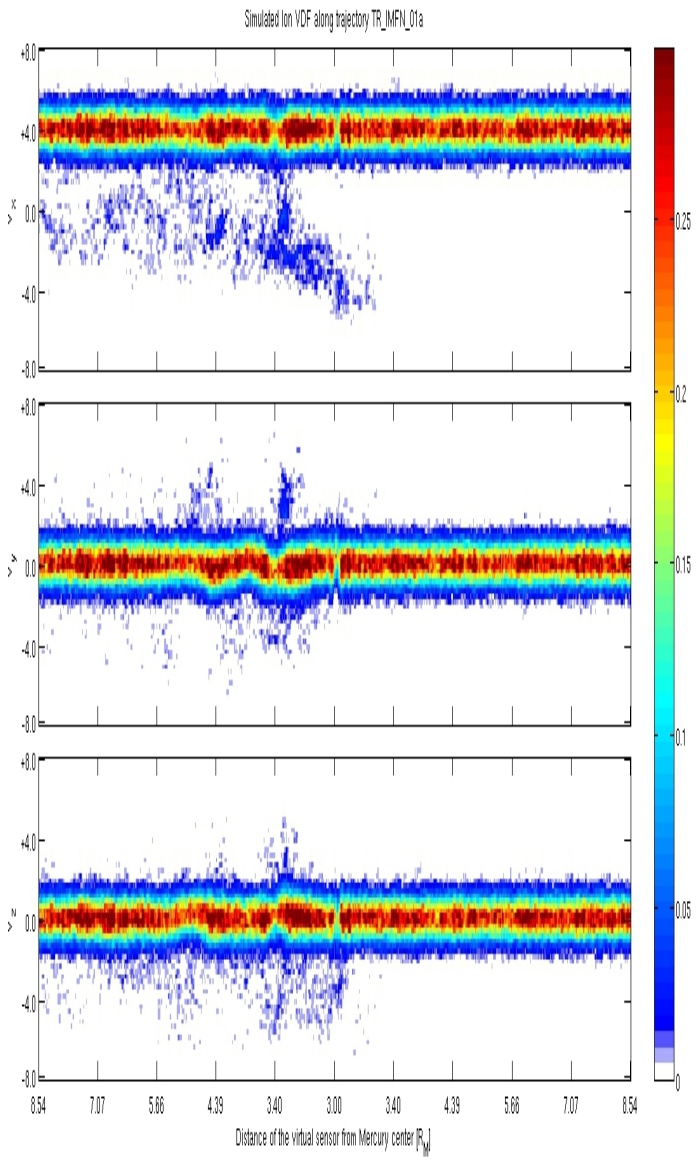
Simulated Ion VDF along trajectory TR_IMFN_01a
V_X
V_Y
V_Z
Distance of the virtual sensor from Mercury center [R_M]

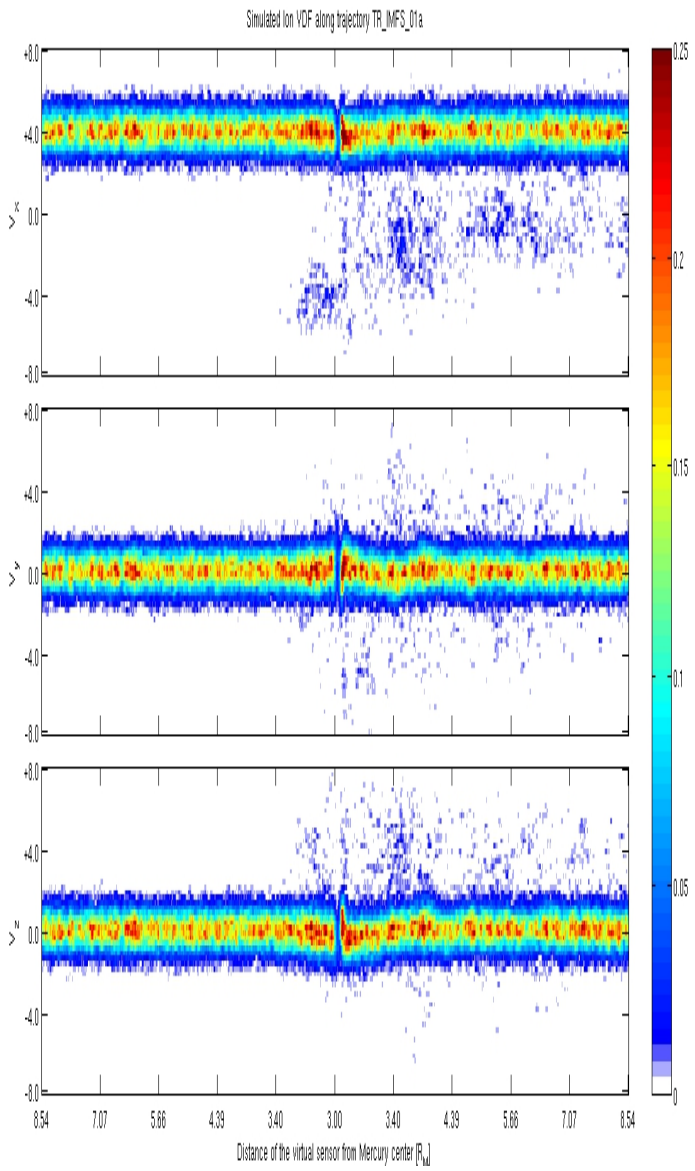
Simulated Ion VDF along trajectory TR_IMFS_01a
V_X
V_Y
V_Z
Distance of the virtual sensor from Mercury center [R_M]

MESSENGER

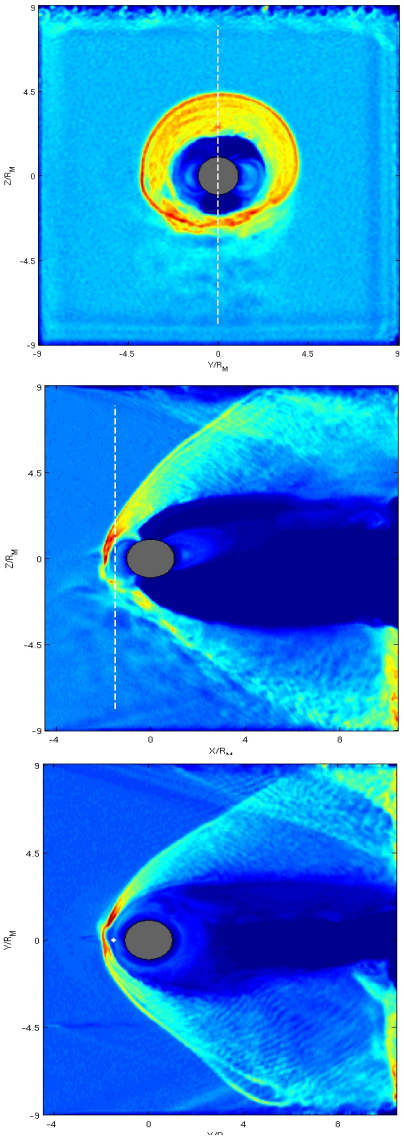

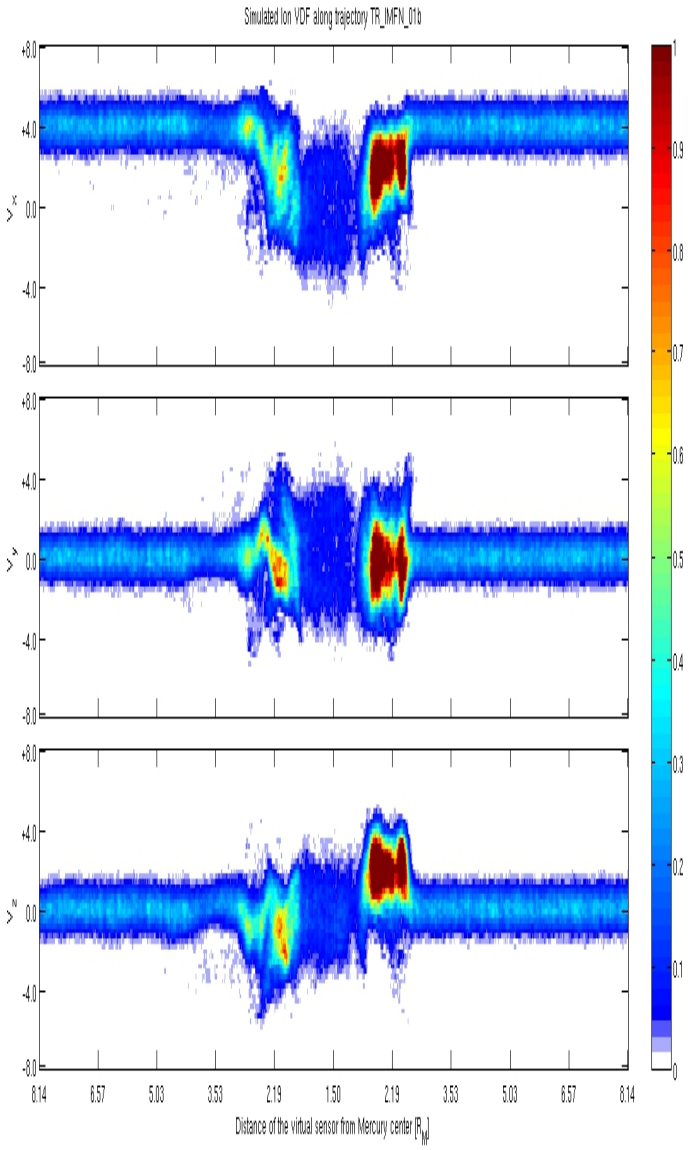
Simulated Ion VDF along trajectory TR_IMFN_01b
Distance of the virtual sensor from Mercury center [R_M]

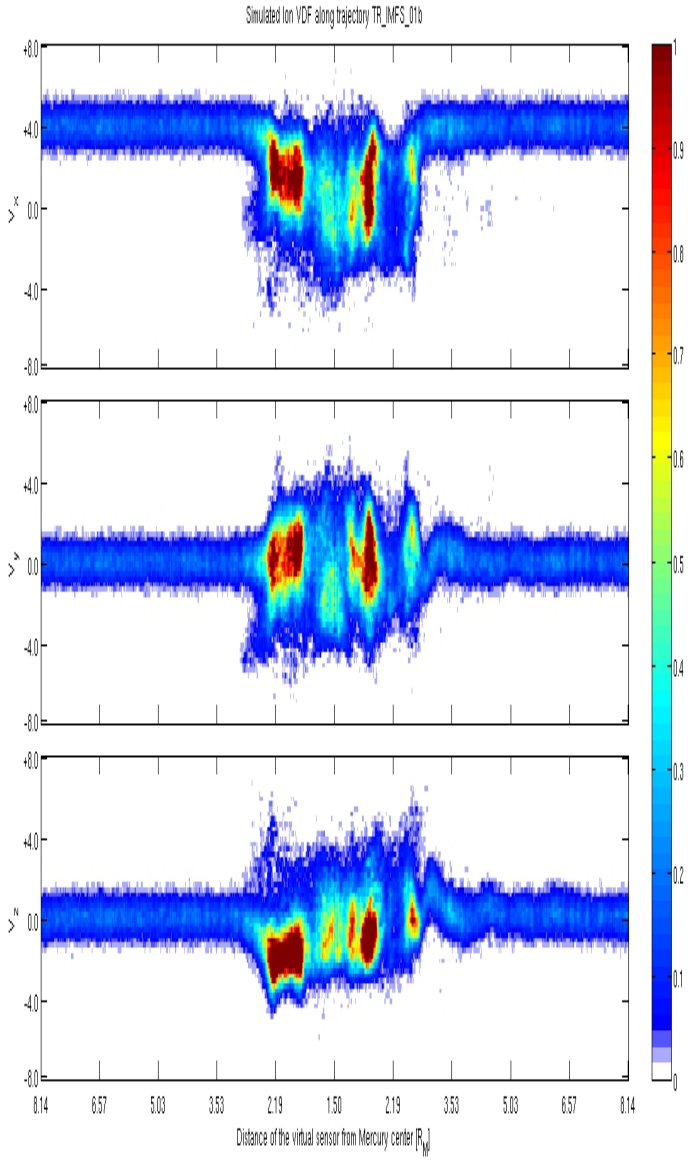
Simulated Ion VDF along trajectory TR_IMFS_01b
Distance of the virtual sensor from Mercury center [R_M]

MESSENGER

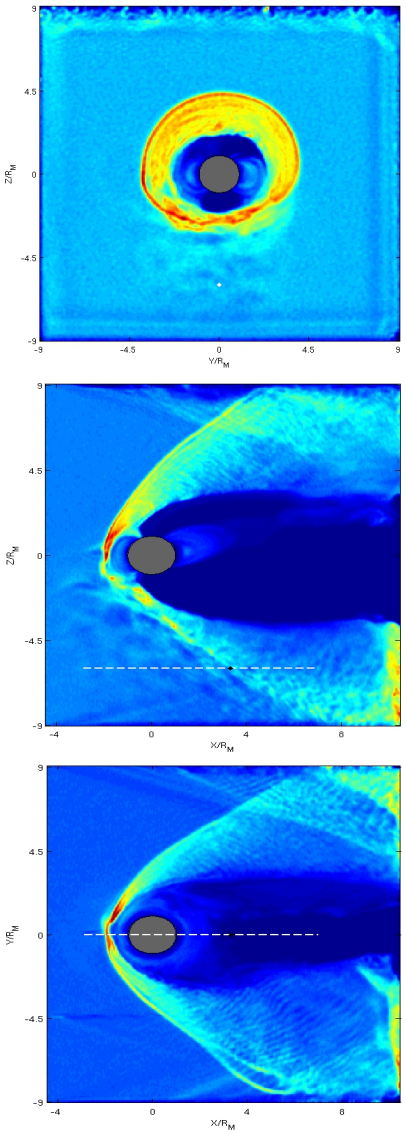
Z/R_M
Y/R_M
X/R_M

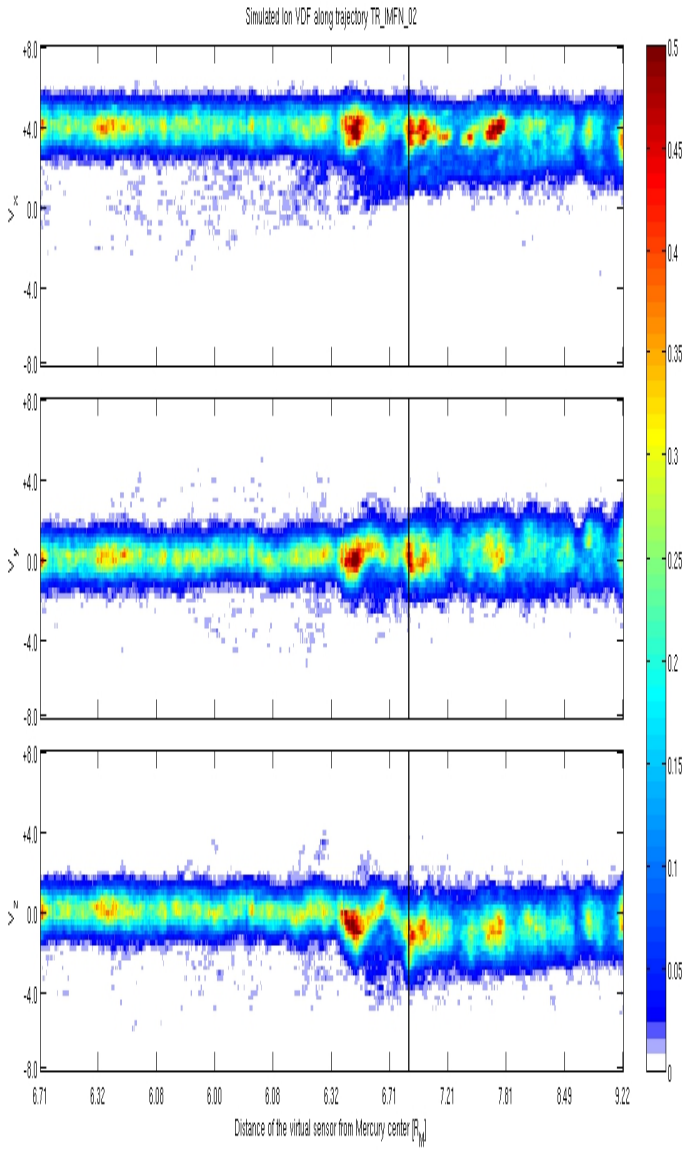
Simulated Ion VDF along trajectory TR_IMFN_02
V_x
V_y
V_z
Distance of the virtual sensor from Mercury center [R_M]

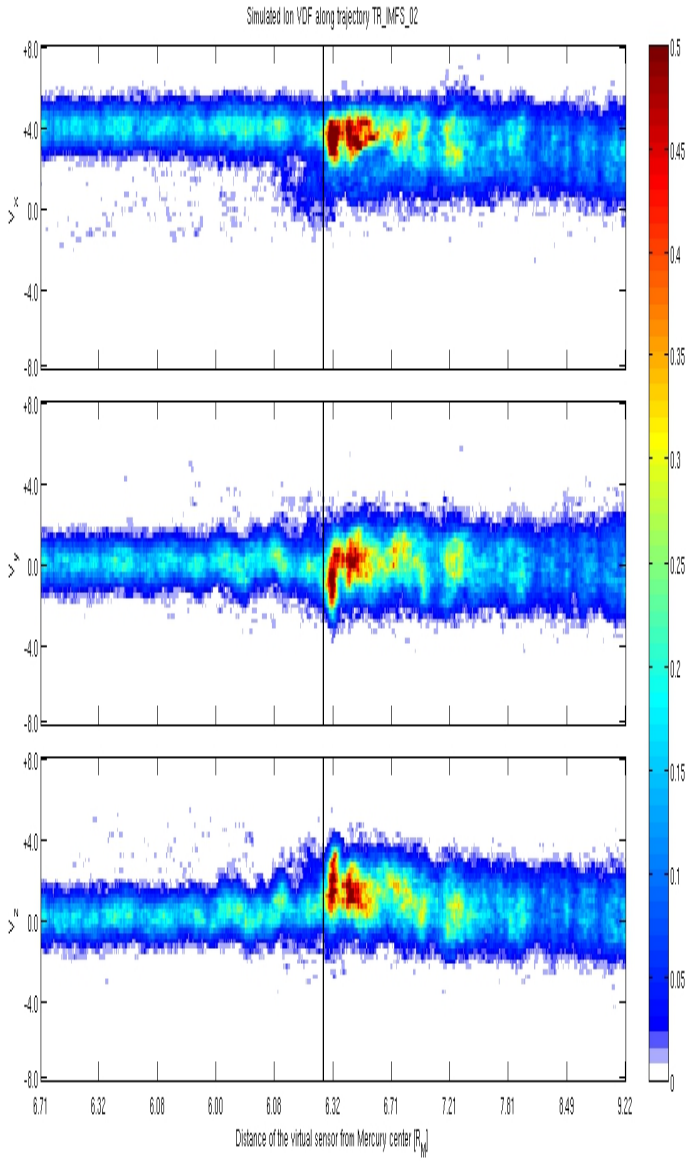
Simulated Ion VDF along trajectory TR_IMFS_02
V_x
V_y
V_z
Distance of the virtual sensor from Mercury center [R_M]

MESSENGER

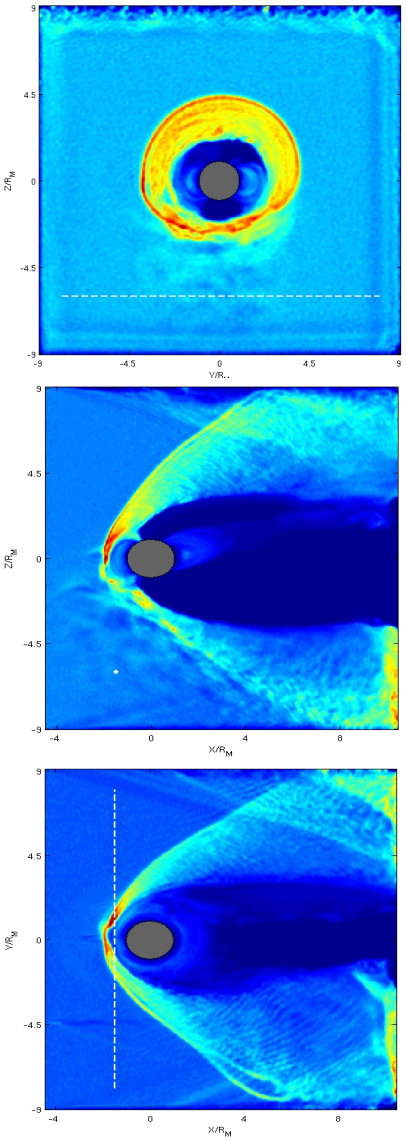
Z/R_M
Y/R_M
X/R_M

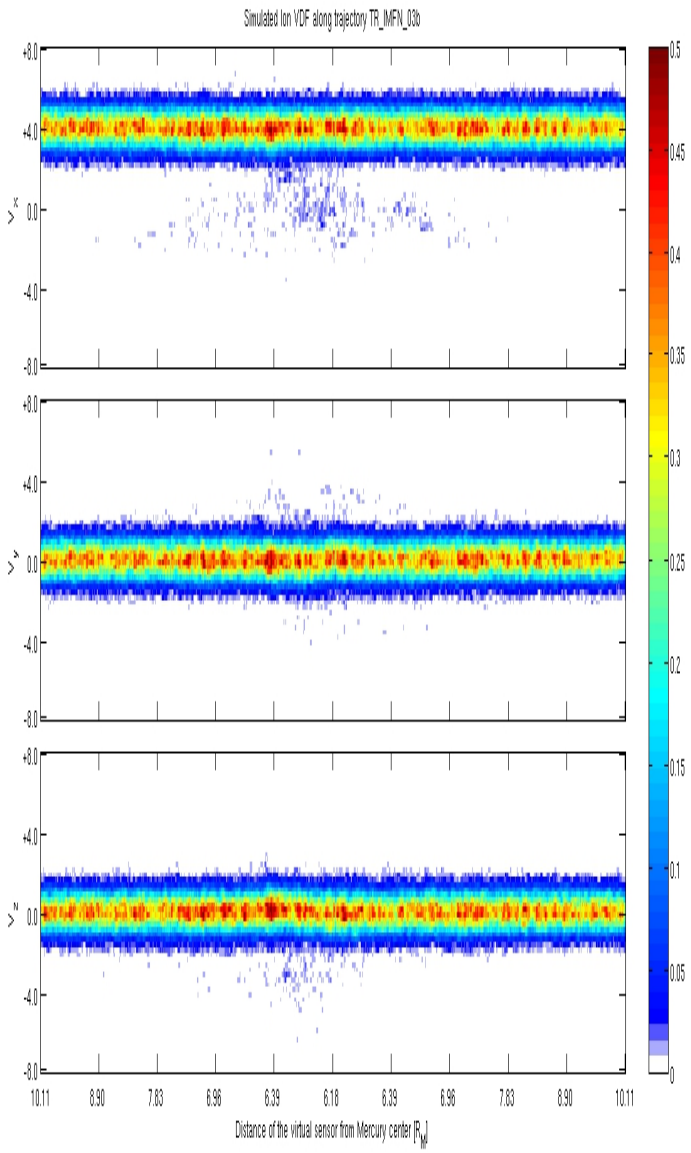
Simulated Ion VDF along trajectory TR_IMFN_03b
V_x
V_y
V_z
Distance of the virtual sensor from Mercury center [R_M]

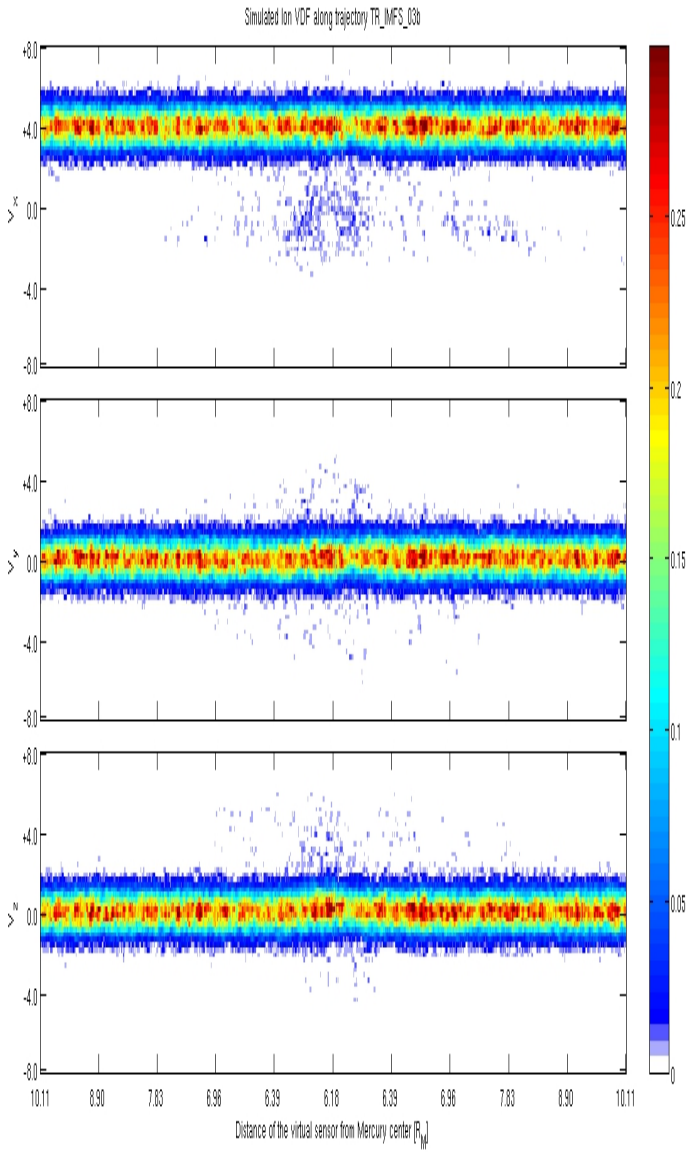
Simulated Ion VDF along trajectory TR_IMFS_03b
V_x
V_y
V_z
Distance of the virtual sensor from Mercury center [R_M]

Summary 1 of 3

- The overall magnetospheric features of the simulated system are similar to those in the terrestrial magnetosphere.
- We observe typical series of thin and thick transition regions appear including bow shock, magnetosheath, magnetopause, magnetotail, magnetosphere itself, plasma belt, etc.
- The simulated results are in a good qualitative agreement with *in situ* observations of MESSENGER.
- The oblique/quasi-parallel bow shock region is a source of backstreaming protons filling the foreshock where they generate strong wave activity.
- These large-amplitude waves are transported with the solar wind to the adjacent magnetosheath.
- In the quasi-perpendicular magnetosheath, waves are generated near the bow shock and locally by the proton temperature anisotropy.

Summary 2 of 3

- For the low-β plasma considered here, the dominant instability in the quasi-perpendicular magnetosheath is the proton cyclotron instability, a result confirmed by the density-magnetic field $\langle n_p, B \rangle$ correlation analysis.
- The positions of the foreshock and the quasi-parallel and quasi-perpendicular bow shock regions are controlled by the IMF orientation.
- Magnetospheric plasma also exhibits a proton temperature anisotropy (loss cone) with a signature of (drift) mirror mode activity.
- For both orientations magnetospheric cusps form on the day side, at higher latitudes for northward IMF compared to southward IMF. The day side magnetosphere has a smaller size for southward IMF. These differences are likely related to different locations of reconnection regions for the two orientations.

Summary 3 of 3

- In the case of southward IMF the night-side magnetospheric cavity in the Z direction is wider. We found strong sunward plasma flows within Mercury's magnetotail. For southward IMF the sunward plasma flows is stronger owing to a presence a strong sunward proton beam, a signature of the reconnection process occured further downtail in the thin current sheet (along with the formation of plasmoids).
- These energetic protons likely contribute to the thermal and dynamic pressure of the magnetospheric plasma widening the magnetospheric cavity in the case of southward IMF.
- Both IMF configurations lead to a quasi-trapped plasma belt around the planet. Such a belt may account for the diamagnetic decreases observed on the inbound passes of both MESSENGER flybys.